AFRL-AFOSR-VA-TR-2022-0030

Controlling resistance degradation of high-permittivty dielectrics by bulk and interface Fermi level engineering

Klein, Andreas
Technische Universität Darmstadt
Jovanka-Bontschits-Str. 2
Darmstadt, Hessen, , 64287
DE

11/19/2021
Final Technical Report

Air Force Research Laboratory
Air Force Office of Scientific Research
Arlington, Virginia 22203
Air Force Materiel Command

REPORT DOCUMENTATION PAGE

Form Approved
OMB No. 0704-0188

1. REPORT DATE *(DD-MM-YYYY)*	**2. REPORT TYPE**	**3. DATES COVERED** *(From - To)*
19-11-2021	Final	01 Jul 2018 - 30 Jun 2021

4. TITLE AND SUBTITLE
Controlling resistance degradation of high-permittivty dielectrics by bulk and interface Fermi level engineering

5a. CONTRACT NUMBER

5b. GRANT NUMBER
FA9550-18-1-0385

5c. PROGRAM ELEMENT NUMBER
61102F

6. AUTHOR(S)
Andreas Klein

5d. PROJECT NUMBER

5e. TASK NUMBER

5f. WORK UNIT NUMBER

7. PERFORMING ORGANIZATION NAME(S) AND ADDRESS(ES)
Technische Universität Darmstadt
Jovanka-Bontschits-Str. 2
Darmstadt, Hessen, 64287
DE

8. PERFORMING ORGANIZATION REPORT NUMBER

9. SPONSORING/MONITORING AGENCY NAME(S) AND ADDRESS(ES)
AF Office of Scientific Research
875 N. Randolph St. Room 3112
Arlington, VA 22203

10. SPONSOR/MONITOR'S ACRONYM(S)
AFRL/AFOSR RTB1

11. SPONSOR/MONITOR'S REPORT NUMBER(S)
AFRL-AFOSR-VA-TR-2022-0030

12. DISTRIBUTION/AVAILABILITY STATEMENT
A Distribution Unlimited: PB Public Release

13. SUPPLEMENTARY NOTES

14. ABSTRACT
Polycrystalline Mn- and Fe-doped BaTiO3 ceramics were synthesized using the solid-state synthesis route with different doping concentration. Resistance degradation is considerably suppressed with increasing doping concentration. In order to quantify defect energy levels, enthalpies of segregation of oxygen vacancies, electrical current, and oxygen migration paths, samples have been strongly reduced in Ar/H2 atmosphere and slowly re-oxidized by temperature cycling in dry air or similar mixtures of 1-20% oxygen with inert gases such as Aror N2. The re-oxidation behavior is monitored by continuously recording the dc electrical conductivity. Substantial differences are observed in dependence on dopant species and concentration, which can partially be related to the different defect energy levels of Mn and Fe. The current paths are obtained from simulations of the electrostatic potential distribution, taking account of the segregation of oxygen vacancies to the grain boundary core following the widely accepted model and procedure introduced by Souza. By comparing the simulations with measured activation energies as a function of conductivity (oxygen vacancy concentration), it should be pos¬sible to extract the energy levels of the defects and the enthalpy of segregation.

15. SUBJECT TERMS

16. SECURITY CLASSIFICATION OF:			**17. LIMITATION OF ABSTRACT**	**18. NUMBER OF PAGES**	**19a. NAME OF RESPONSIBLE PERSON**
a. REPORT	**b. ABSTRACT**	**c. THIS PAGE**			ALI SAYIR
U	U	U	UU	23	**19b. TELEPHONE NUMBER** *(Include area code)* 426-7236

Standard Form 298 (Rev.8/98)
Prescribed by ANSI Std. Z39.18

Final Report

Project:

Controlling resistance degradation of high-permittivity dielectrics by bulk and interface Fermi level engineering

Funded by Air Force Office of Scientific Research

Grant number: FA9550-18-1-0385

Technische Universität Darmstadt, Karolinenplatz 5, Darmstadt 64289, Germany

Project leader

Prof. Dr. Andreas Klein

Technische Universität Darmstadt, Department of Materials and Earth Science,

Electronic Structure of Materials, Otto-Berndt-Str. 3, Darmstadt 64287, Germany

aklein@esm.tu-darmstadt.de

Contributors:

M.Sc. Katharina Schuldt, M.Sc. Lisanne Gossel, M.Sc. Hui Ding,

M.Sc. Baris Öcal, B.Sc. Nicola Gutmann, Dr. Issei Suzuki, M.Sc. Binxiang Huang

Abstract

Polycrystalline Mn- and Fe-doped $BaTiO_3$ ceramics were synthesized using the solid-state synthesis route with different doping concentration. Resistance degradation is considerably suppressed with increasing doping concentration. In order to quantify defect energy levels, enthalpies of segregation of oxygen vacancies, electrical current, and oxygen migration paths, samples have been strongly reduced in Ar/H_2 atmosphere and slowly re-oxidized by temperature cycling in dry air or similar mixtures of 1-20% oxygen with inert gases such as Ar or N_2. The re-oxidation behavior is monitored by continuously recording the dc electrical conductivity. Substantial differences are observed in dependence on dopant species and concentration, which can partially be related to the different defect energy levels of Mn and Fe. The current paths are obtained from simulations of the electrostatic potential distribution, taking account of the segregation of oxygen vacancies to the grain boundary core following the widely accepted model and procedure introduced by Souza. By comparing the simulations with measured activation energies as a function of conductivity (oxygen vacancy concentration), it should be possible to extract the energy levels of the defects and the enthalpy of segregation. The simulations for Mn-doped $BaTiO_3$ show partial agreement with experiments, confirming the assumed defect energy levels and suggesting a small enthalpy of segregation. However, some aspects of the measurements of the Mn-doped samples are not captured by the simulations and those of the Fe-doped samples differ substantially from the predicted behavior. It is suggested that additional aspects have to be included in the simulations. Among them are the temperature dependence of space-charge regions, the segregation of cation vacancies and dopants to the grain boundary core, and variation of the oxygen content throughout the sample thickness. The Schottky barrier heights at $BaTiO_3/RuO_2$ and at $BaTiO_3$/ITO interfaces have been analyzed by means of X-ray photoelectron spectroscopy for $BaTiO_3$ samples with different Mn and oxygen vacancy concentrations. No pinning of the Fermi level at the Mn defect energy levels has been observed. This is related to the high permittivity of the sample, which results in a wide extension of the space-charge region in $BaTiO_3$. The high permittivity of $BaTiO_3$ thus enhances the influence of space-charge regions on the electrical properties.

Motivation and objectives

The goal of the project was to derive a quantitative understanding of the Fermi energy and the electrostatic potential distribution at grain boundaries and electrode interfaces and their influence on resistance degradation of multilayer ceramic capacitors, which limits their application at elevated temperature [1][2]. Grain boundaries are known to suppress resistance degradation as they block oxygen migration due to the presence of space-charge regions, in which the concentration of oxygen vacancies is reduced [3]. On the other hand, space-charge regions at electrode interfaces will affect oxygen transport towards the electrode, where oxygen might react with the electrodes or where it can be incorporated or extracted from the dielectric [4][5]. Thereby, the overall oxygen vacancy concentration in the dielectric can change when high voltages are applied at high temperature. In order to quantify space-charge regions, the Fermi energy in the bulk and at interfaces has to be quantified. While the latter is straightforward by means of photoelectron spectroscopy, the Fermi energy in the bulk is not directly accessible. To address this, it has been elaborated to which extend the defect energy levels can be determined from the activation energy of electrical conductivity as a function of the oxygen vacancy concentration in polycrystalline acceptor-doped $BaTiO_3$ bulk ceramics. This procedure has been demonstrated for single crystalline $SrTiO_3$ and $BaTiO_3$ [6]. However, polycrystalline materials are used in standard multilayer capacitors. The current flow

across and along grain boundaries will affect the activation energy, preventing a direct determination of the defect energy levels from the activation energy in polycrystalline material. Therefore, simulations of current flow considering an electrostatic potential distribution inside the grains have been required and setup. The simulations are based on the model suggested by De Souza [7] and has been extended to extract the conduction along grain boundaries. By comparison with experiment, it should also be possible to estimate the enthalpy of segregation of oxygen vacancies, which is an important parameter to quantify the influence of grain boundaries.

Another approach to identify defect energy levels is to identify potential Fermi level pinning at defect energy levels. Such a pinning may be observed from a dependence of the Fermi energy at the electrode interface (Schottky barrier height) on the defect concentration [8]. A pinning of the Fermi energy at the electrode interface will also affect the space-charge region. This is widely used in semiconductor technology for the engineering of energy band alignment and has the potential to control the oxygen exchange at the electrode interface. Identification of Fermi level pinning requires a systematic study of the influence of defect concentrations. We have determined the Schottky barrier height in dependence on the Mn concentration. In addition, we have varied the oxygen vacancy concentration by means of using reduced, equilibrated and oxidized $BaTiO_3$ samples. The Fermi energy at the interface was furthermore varied by using RuO_2 and ITO (Sn-doped In_2O_3) as contact materials.

Results

1 Preparation of polycrystalline $BaTiO_3$ ceramics

The Fermi energy in $BaTiO_3$ is determined by the defect equilibria and follows from the doping concentrations, the concentration of oxygen vacancies and from the defect energy levels of the involved defects. In order to study the influence of these parameters, Mn- and Fe-doped $BaTiO_3$ bulk ceramic samples have been synthesized using conventional solid-state reaction method. The synthesis was supported by Dr. Jurij Koruza from the Non-metallic Inorganic Materials (NAW) group of the Materials Science Department at Technical University of Darmstadt. Mn-doped samples with 0.05, 0.1, 0.2, 0.3, 0.4, 0.5, and 0.6 wt.% $MnCO_3$ have been synthesized. Further samples were doped 0.1 and 0.5 wt.% Fe_2O_3.

X-ray diffraction patterns of calcined powders (Figure 1) confirmed the absence of secondary phases but revealed the presence of a hexagonal $BaTiO_3$ phase for higher Mn concentrations, which agrees with reports in literature [9]. The dielectric properties, which are important for the evolution of space-charge regions at grain boundaries and at electrode interfaces are displayed in Figure 2. In agreement with literature reports [10], the addition of acceptors reduces the permittivity and lowers the Curie point of the samples. The reduction of the Curie point is much more pronounced for the Fe-doped samples, for which a 0.5 wt.% doping concentration lowers the Curie point from 130 °C to 90 °C. For Mn-doping, the same doping concentration results in a lowering of T_C by only 5 K.

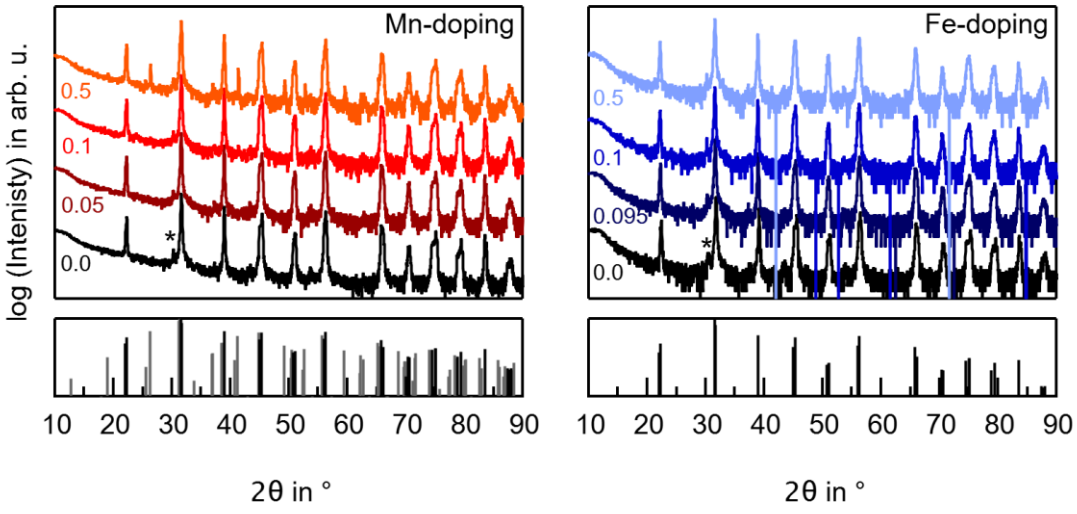

Figure 1: XRD pattern of the calcined powders: The patterns were recorded by a D8 Advance diffractometer from Bruker AXS with Cu Kα radiation filtered by a Sol-X detector. The reflection marked with * at 30.22° corresponds to an artificial tungsten reflex, which results from the X-ray tube. In the lower panel the powder diffraction pattern of BTO [01-082-1175] - hex. - P63/mmc (grey), ICSD collection code: 075240 and BTO [01-081-2201] - tetr. - P4mm (black), ICSD collection code: 073642 are displayed.

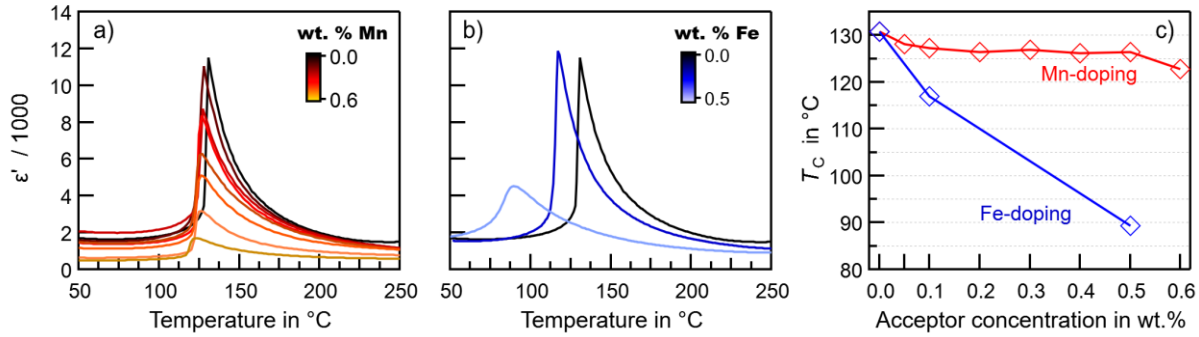

Figure 2: a) and b) Real part of the permittivity ε' at 1000 Hz as a function of temperature during the first heating cycle for untreated acceptor-doped BaTiO3 ceramic samples. All samples were measured with Pt electrodes and a heating rate of 2K/min. The measurements were conducted on a Hewlett Packard 4284A Precision LCR- Meter (Hewlett Packard Enterprise,USA). c) Determined Curie point for a frequency of 1000 Hz.

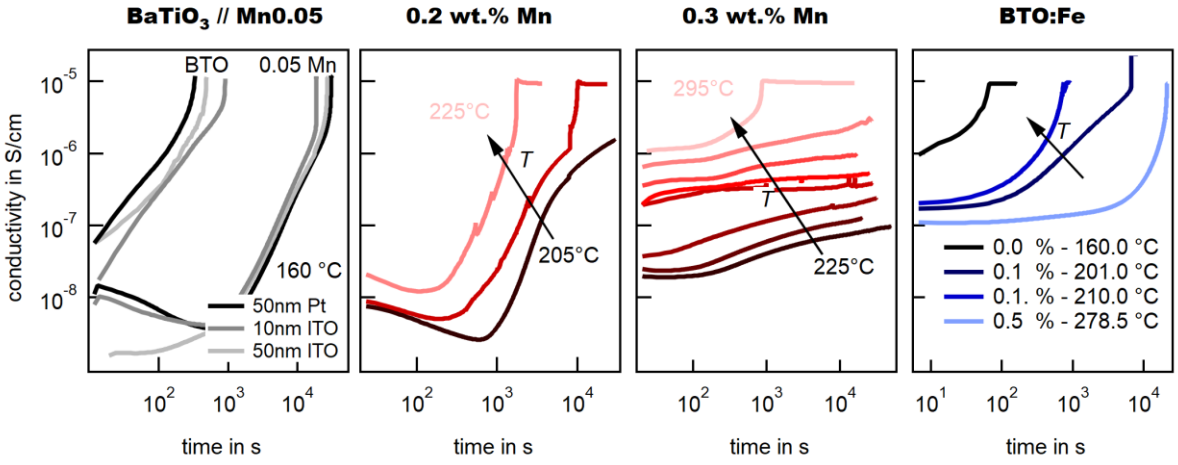

Figure 3: Degradation curves of acceptor-doped $BaTiO_3$ ceramics. A constant electric field of 0.3 kV/mm was applied. Pt-electrodes were used if not otherwise stated. For intentionally undoped and 0.05 wt.% Mn-doped BTO the anode material (Pt or ITO) and thickness were varied. For higher doping concentrations the sample temperature was increased in order to achieve a reasonable degradation time. The sample temperature is assumed to be homogeneous before starting the measurement.

2 Resistance degradation measurements

Resistance degradation of samples equilibrated in air at 900 °C was studied by home-made setups at different temperatures. For this purpose, pellets of 7-8 mm diameter and 0.4-0.5 mm thickness were sputtered with 50 nm thick Pt electrodes unless otherwise noted. An electric field of 0.3 kV/mm was applied on all samples. The results of the degradation measurements are shown in Figure 3. The samples were degraded at different temperatures to obtain similar degradation times.

The degradation curves are different from those reported for single crystalline $SrTiO_3$ [11]. Undoped samples exhibited the fastest degradation. At a substrate temperature of 160 °C, the samples reach the current compliance of the setup, which corresponds to an electrical conductivity of 10^{-5} S/cm, after less than 100 s. Adding only 0.05 wt.% of Mn already increases the degradation time to above 10^4 s at the same

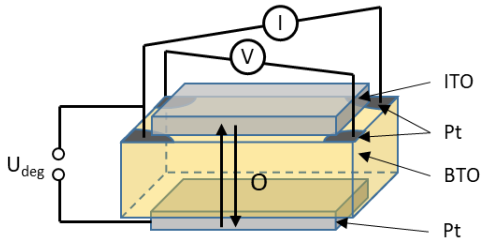

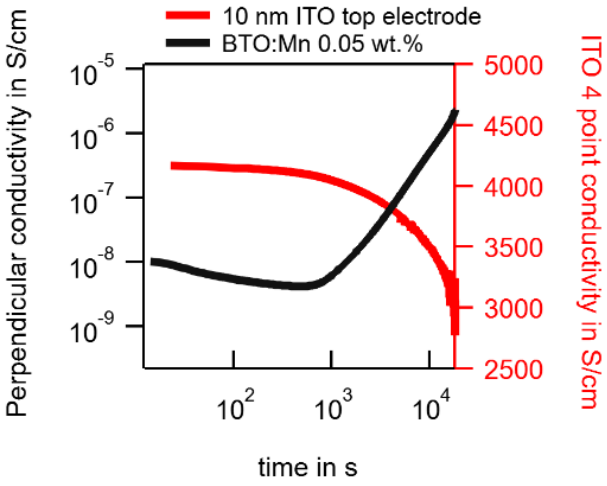

Figure 4: Experimental configuration (top) and electrical degradation and electrode conductivity (right) of a 0.05 wt. % Mn-doped $BaTiO_3$ ceramic with a Pt cathode and a 10 nm ITO anode. The 4-point conductivity of the ITO anode is displayed in red. A constant electric field of 0.3 kV/mm was applied at a sample temperature of 160 °C.

In contrast to what has been reported in the final report of the preceding project (FA9550-14-1-0158), there seems to be no influence of the electrode on the resistance degradation. In particular, degradation appeared to be absent if thin ITO electrodes have been used as an anode during degradation. In the left graph of Figure 3 the degradation curves of nominally undoped and of 0.05 wt.% Mn-doped samples with 50 nm thick Pt, and with 10 and 50 nm thick ITO anode electrodes are displayed. All samples exhibited comparable degradation behavior. The differences to the previous measurements can be explained by the lower electrode thicknesses used in the previous studies. To confirm this, we have measured the conductivity of a 10 nm thick ITO anode during degradation. As shown in

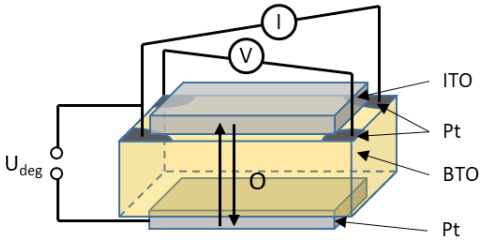

temperature. The more Mn is added, the more the degradation time increases. With 0.2 wt.% Mn doping, the temperature has to be increased to above 200°C. At 225°C, the conductivity limit is reached after 2000 s. With 0.3 wt.% Mn doping and a temperature of 295°C the current compliance is reached to in less than 10^4 s. For higher doping concentration, the temperature has to be increased that much, that the conductivity is already too high before degradation starts. The reduced conductivity degradation with increasing Mn concentration is in-line with that reported by Yoon *et al.* [12]. The situation is similar for the Fe-doped samples, but the degradation of the Fe-doped samples is faster than that of the Mn-doped ones. A 0.5 wt.% Fe-doped sample still degrades at 280 °C, while no degradation could be observed for same concentration of Mn. According to our defect simulations, this difference is related to the different energy levels of the Mn and Fe, which emphasizes the importance of quantifying the defect energy levels of the dopants.

Figure 4, the conductivity of the ITO electrode evidently decreases during degradation. This is explained by incorporation of oxygen from $BaTiO_3$ into the ITO, when this is used as anode (positively charged oxygen vacancies are migrating towards the cathode during degradation. If the ITO electrode is too thin, its conductivity will be reduced that much, that it does not serve as electrical contact anymore. The

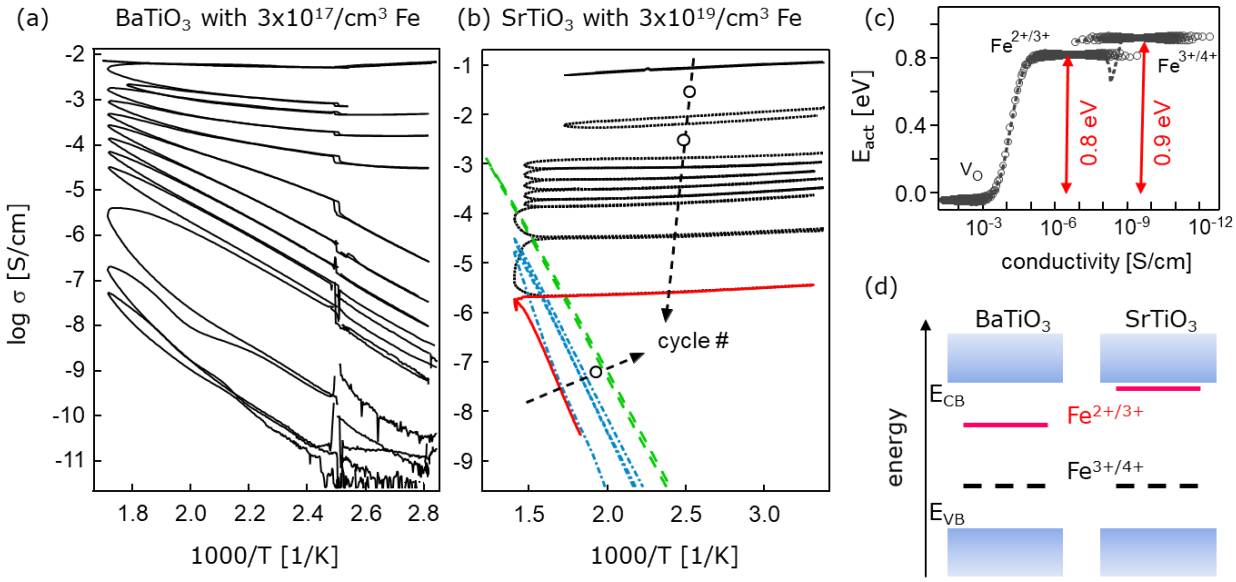

Figure 5: Re-oxidation of a reduced nominally undoped $BaTiO_3$ single crystal (a) and of a 0.05 wt.% Fe-doped $SrTiO_3$ single crystal (b). Panel (c) shows the calculated activation energy of electronic conductivity as a function of the sample's conductivity at 200 °C assuming that the $Fe^{3+/4+}$ charge transition is located 0.9 eV above the valence band maximum and the $Fe^{2+/3+}$ charge transition at 0.8 eV below the conduction band minimum. Panel (d) displays the energy level diagram of Fe impurities in $BaTiO_3$ and $SrTiO_3$. The results are published in [6].

excorporation of oxygen at the positive electrode can even lead to the formation of gas bubbles in the case of Pt electrodes [5].

3 Determination of defect energy levels from re-oxidation of reduced $SrTiO_3$ and $BaTiO_3$ single crystals

In order to derive the bulk Fermi energy in the materials, it is necessary to quantify the defect energy levels (the charge transition levels) of the involved defects. In semiconductor physics, these can be obtained from the activation energy of temperature dependent conductivity measurements. In oxide ceramics, the conductivity is often too low and the number of defects, in particular that of oxygen vacancies, can vary depending on processing. Starting at the end of the preceding project, we have developed a novel approach for deriving the defect energy levels by a gradual re-oxidation of reduced crystals. This approach is particularly feasible for $SrTiO_3$ and $BaTiO_3$, which become high electronically conducting upon reduction. The stepwise re-oxidation is performed by repeated temperature cycles in air. One can then follow the activation energy in dependence on the re-oxidation state and compare the result with calculations of conductivity in dependence on oxygen vacancy concentration. These calculations (see Figure 5(c)) reveal that the energy will develop a plateau when plotted in dependence on conductivity. The energy of the plateau does then correspond to the activation energy. Figure 5 shows the re-oxidation measurement of a nominally undoped $BaTiO_3$ single crystal and of $SrTiO_3$ single crystal doped with 0.05 wt.% Fe, respectively.

The re-oxidation behavior is strikingly different for $BaTiO_3$ and $SrTiO_3$. $BaTiO_3$ exhibits a positive activation energy (usually called semiconducting behavior) already after the first oxidation cycle with a gradual increase of the activation energy and a plateau of the activation energy at 0.8 eV. In contrast, the $SrTiO_3$

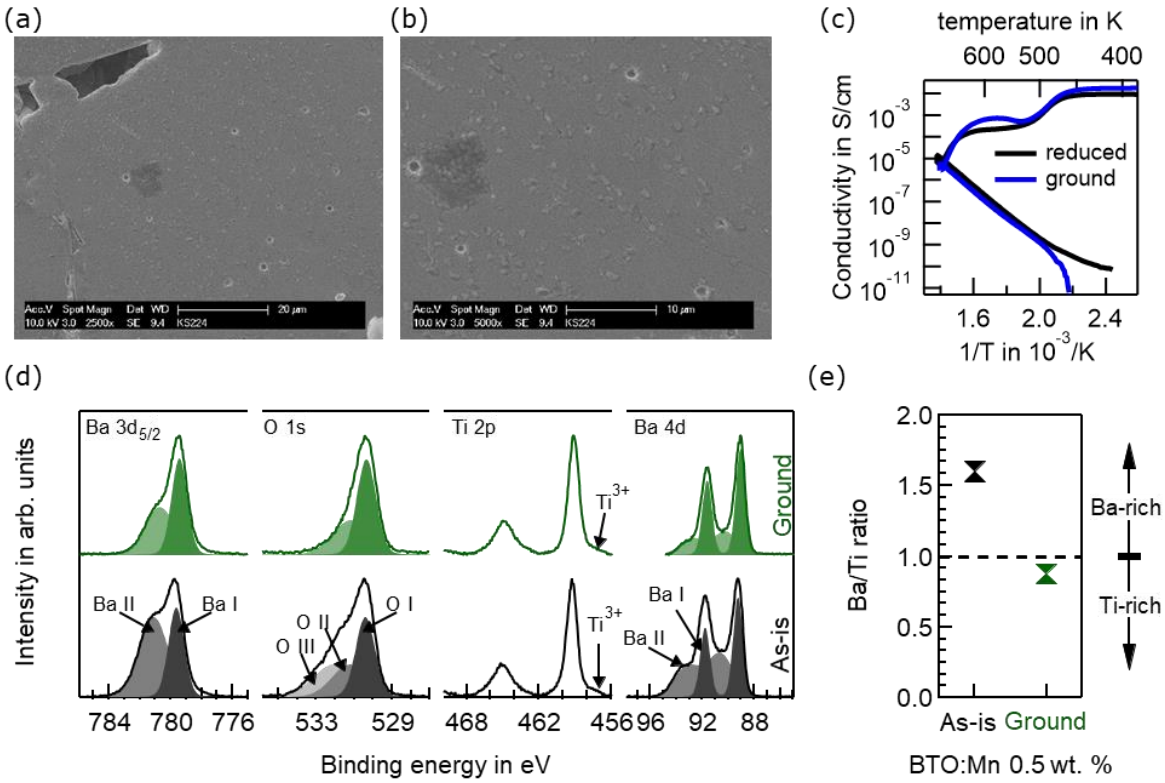

Figure 6: Scanning electron microscopy (SEM) pictures of a reduced 0.5 wt. % $BaTiO_3$ sample conducted with a Philips XL30-FEG (a) and (b). An acceleration voltage of 10 kV, a spot size of 4 and a magnification of 2500 x (a) and 5000 x (b) were used; Temperature dependent conductivity measurements of 0.5 wt. % $BaTiO_3$ samples before (black) and after (blue) removal of the surface layer by grinding (c). Pt electrodes were used for both samples. The samples were slowly heated to 450 °C, hold for one hour and then cooled down to room temperature. Conductivities < 10^{-10} S/cm are uncertain due to the sensitivity limit of the setup. Normalized photoelectron core level spectra of a reduced 0.5 wt.% Mn-doped $BaTiO_3$ ceramic before (black) and after (green) removal of the surface layer by grinding (d). Background subtraction and normalization were performed for better comparison. Curve fitting was conducted for Ba and O emissions using Gauß-Lorentz functions. The derived Ba/Ti ratio calculated with the Ba 3*d* emission is shown for both samples in (e). Except for panel (c), results are published in [13].

sample shows a negative activation energy (metallic behavior) and a sudden strong increase at a conductivity of about 10^{-6} S/cm. Subsequent oxidation cycles showed an increase of conductivity, indicating a dominating p-type conductivity. The different behavior of $BaTiO_3$ and $SrTiO_3$ can be explained by different $Fe^{2+/3+}$ charge transition level, which is about 0.8 eV below the conduction band in $BaTiO_3$ and close to the conduction band in $SrTiO_3$. This result, which is published in [6], is consistent with other experimental studies but only partially consistent with state-of-art defect calculations (see discussion in [6]). It is not expected that the different charge transition level is related to the different Fe concentrations. Further credit for this will be obtained from the defect energy levels extracted from the re-oxidation experiments of polycrystalline Fe-doped $BaTiO_3$ bulk ceramics, which will be described below.

4 Re-oxidation measurements of polycrystalline acceptor-doped $BaTiO_3$

4.1 Analysis of reduced samples

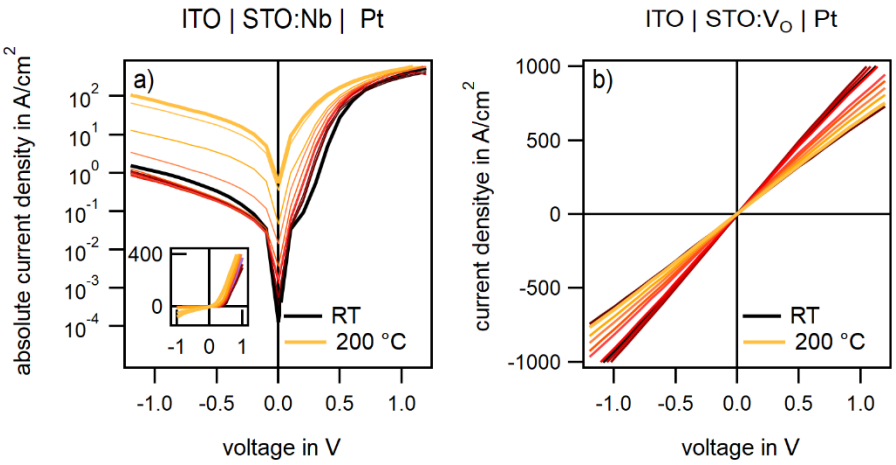

Figure 7: Current density as a function of voltage for a) Nb-doped $SrTiO_3$ (STO:Nb) and b) reduced $SrTiO_3$ (STO:V_O) single crystals with ITO back electrodes and Pt working electrodes. The STO:V_O was reduced for at least 12 h at 1100 °C in 5% H_2/95% Ar and quenched back to room temperature by a fan to archive a considerably high V_O concentration. The temperature was varied from room temperature (black) to 200 °C (orange) in 50 °C steps.

At the beginning of each re-oxidation experiment, the samples were reduced for at least 12 h at 1100 °C in 5% H2/95% Ar and rapidly cooled to room temperature by a fan cooling. The surfaces were polished with 1 µm diamond paste finish before reduction. XPS analysis revealed a clear effect of the reduction on surface composition (see Figure 6(d), (e)). The surface feature of the Ba 3*d* and Ba 4*d* emissions (Ba II) is strongly enhanced. Also an additional oxygen component is observed. Both are associated with the formation of BaO on the surface, which is further confirmed by the strong enhancement of the Ba/Ti ratio measured by XPS at reduced surfaces (see Figure 6(e)). After removing the surface layer by grinding, the $BaTiO_3$ stoichiometry is re-established but the sample is still strongly reduced as evident from the presence of a Ti^{3+} component before and after grinding. It remains unclear, however, why the reduction results in the formation of a BaO surface layer. Typically, the segregation of *A*-site cations to the surface, which follows the formation of *A*-site vacancies is expected to be favored for oxidizing conditions [14]. A more detailed discussion of the surface composition of reduced $BaTiO_3$ is given in [13].

Although the surface composition is strongly affected by the reduction treatment, the re-oxidation measurements are not expected to be affected by the surface BaO layer, as the electrical conduction is dominated by bulk properties. This assumption is confirmed by the comparison of single-step re-oxidation experiments of a 0.5 wt.% Mn-doped samples with BaO surface layer with that of a sample were the surface layer has been removed. As shown in Figure 6(c), the two curves are largely identical.

The used Pt contacts may exhibit high Schottky barriers on $BaTiO_3$, which may influence the re-oxidation experiments as these are carried out in 2-point configuration. High Schottky barriers are particularly expected in the course of re-oxidation [15]. In order to exclude an influence of barrier heights, we have performed current-voltage measurements of Schottky diodes prepared with a reduced and with a Nb-doped $SrTiO_3$ single crystal. ITO has been used as ohmic contact and Pt as Schottky contact. While the Nb-doped $SrTiO_3$ exhibits a clear rectifying behavior as expected from the different work functions of the two electrode materials [16], the reduced crystal exhibits linear and symmetric properties, indicating ohmic contact behavior of both electrodes. The difference is explained by mobile oxygen vacancies [17]. The upward band bending at the Pt contact accumulates oxygen vacancies and thereby increases the effective

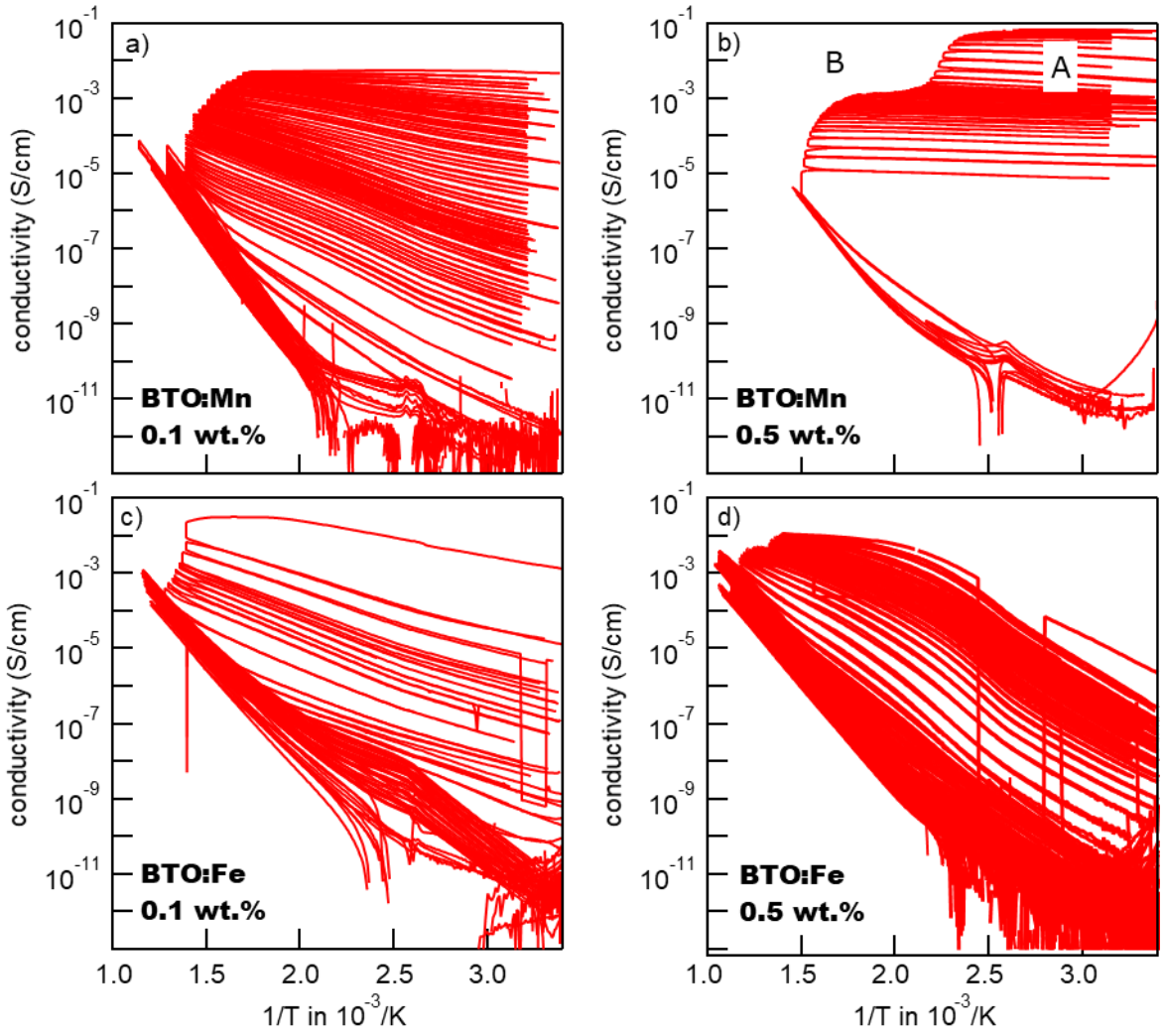

Figure 8: Temperature dependent conductivity measurements of Fe- and Mn-doped $BaTiO_3$ ceramics. All samples were reduced for at least 12 h at 1100 °C in 5% H_2/95% Ar and quenched back to room temperature by a fan. Pt electrodes were used for all samples. The samples were slowly heated to a certain dwell temperature, hold for a certain dwell time and then cooled down. This results in a stepwise re-oxidation of the samples. All graphs are identically scaled for better comparison.

doping density in the space-charge region. Eventually, the space-charge region at the contact becomes narrow enough for electrons to tunnel through the barrier, leading to an ohmic contact behavior. As there is no significant concentration of oxygen vacancies in Nb-doped $SrTiO_3$, the doping concentration remains constant in the space-charge region and the electrons have to overcome the barrier, leading to a rectifying current-voltage characteristic.

4.2 Stepwise re-oxidation

Stepwise re-oxidation experiments of 0.1 and 0.5 wt.% Mn- and Fe-doped $BaTiO_3$ are shown in Figure 8. The re-oxidation behavior clearly depends on both, the nature of the dopant and on its concentration. The following observations can be extracted:

i. The room temperature conductivity of the Fe-doped samples is lower than that of the Mn-doped samples, particular for the higher doped films. This difference is related to the different energy

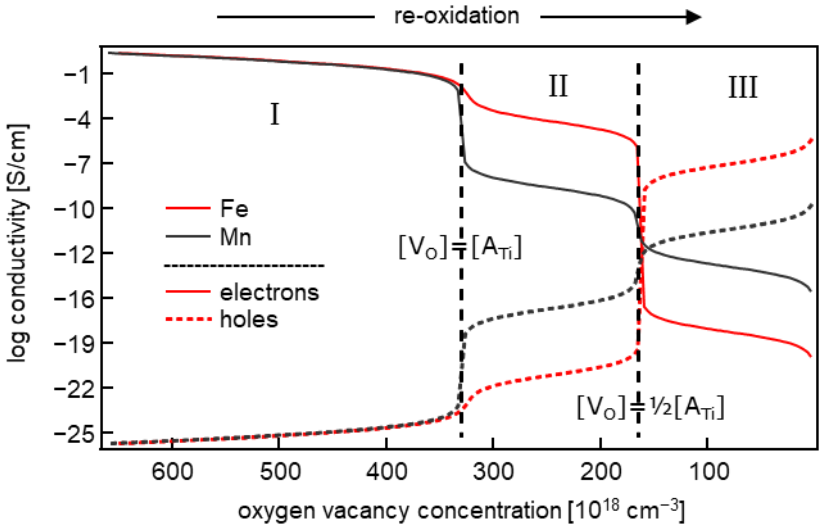

Figure 9: Electronic conductivities of $BaTiO_3$ doped with 0.5 wt.% Fe or Mn as a function of oxygen vacancy concentration at 400 °C. The different regions are related to:

I: $[V_O] > [(Fe,Mn)_{Ti}]$
II: $[(Fe,Mn)_{Ti}] > [V_O] > ½ [(Fe,Mn)_{Ti}]$
III: $[V_O] < ½ [(Fe,Mn)_{Ti}]$

No grain boundaries are considered in the calculation.

level of the 3+/2+ transition, which occurs at 1.9 eV above the valence band maximum for Mn and at 2.4 eV for Fe [18]. As the charge transition level of Mn is lower than that of Fe, Mn is easier to reduce. This is confirmed by defect chemical calculations, which reveal that the oxygen vacancy concentration is slightly higher than the acceptor concentration in Mn-doped samples and slightly lower than in Fe-doped samples. The dependence of the oxygen vacancy concentration on defect energy levels is a pre-requisite for the determination of defect energy levels from thermogravimetric studies, which has been done for acceptor-doped $BaTiO_3$ by Hagemann and Hennings [19].

ii. The re-oxidation of the Mn-doped samples seems to occur at lower temperatures as compared to the re-oxidation of the Fe-doped samples. This observation is misleading, however. As shown in Figure 9, the conductivity can be separated into three regions, which are determined by the oxygen vacancy concentration relative to the acceptor concentration. After reduction, the Mn-doped samples clearly belong to region I, in which the oxygen vacancy concentration is higher than the acceptor concentration. Most of the Mn acceptors are in the 2+ oxidation state. In contrast, the Fe-doped samples have a lower conductivity after reduction and are located in region II or at the transition between region I and II, in which the oxygen vacancy concentration is slightly lower than the acceptor concentration and most of the Fe is in the 3+ oxidation state.

In region II, the conductivity of the Fe-doped samples is more than four orders of magnitude higher than that of the Mn-doped ones. This is also a consequence of the $Fe^{2+/3+}$ level being 0.5 eV closer to the conduction band minimum than the $Mn^{2+/3+}$ level. Hence, the observed re-oxidation of the Mn-doped samples corresponds to a transition from region I to region II, while that of the Fe-doped samples corresponds to a transition from region II to region III. It is also noted that the transition from region II to region III may hardly be noticeable, as the conductivity in the 2 regions does not differ much. The electron and hole conductivities are similar in region III for the Mn-doped samples. The same is true for the activation energies, as the distance of the $Mn^{2+/3+}$ level to the conduction band, which dominates the activation energy in region II, is the same as the distance of the $Mn^{3+/4+}$ level to the valence band, which determines the activation energy in region

III. The situation is different for Fe. Here, the activation energies are also similar in the two regions but p-type conduction clearly dominates over n-type conduction in region III.

iii. The 0.1 wt.% Mn-doped sample exhibits a gradual increase of the activation energy, while the 0.5 wt.% doped sample exhibits a negligible activation energy for conductivities down to 10^{-5} S/cm followed by an abrupt increase in activation energy to 1.2 eV. The origin of the noticeably different re-oxidation behavior of the 0.1 and the 0.5 wt.% Mn-doped samples is currently not clear. It might be related to a different kinetics of re-oxidation. On the one hand, the grain size of the samples is substantially reduced with increasing doping concentration from > 10 µm to < 1 µm grain size. On the other hand, the width of the space-charge regions at the grain boundaries is reduced with increasing doping (see simulations below). As oxygen vacancies are depleted in the space-charge region, the diffusivity of oxygen is suppressed therein. The wider space-charge regions may therefore result in longer times required to equilibrate the oxygen content throughout the whole sample.

iv. The 0.5 wt.% Mn-doped sample exhibits a step-like reduction of conductivity from 0.1 S/cm in region A to 10^{-3} S/cm in region B at around 200°C without changing the activation energy of conductivity (Figure 8(b)). This step is also observed in the single-step re-oxidation experiments shown in Figure 6(c) and has been reproduced several times. It may be that the grain boundaries constitute the dominant conduction path in region B while both grain boundaries and grains contribute equally to the total conductivity in region A. However, we do not observe a step-like reduction of conductivity in our simulations (see below), which takes electrical conduction in the grains and at grain boundaries into account. Therefore, we can presently not conclude about the origin of this phenomenon.

v. For the reduced Fe-doped samples, the temperature dependent conductivities saturate above 500 K at $\sigma = 0.01 - 0.1$ S/cm. At these temperatures, the conductivity is comparable to that of the reduced Mn-doped sample. The saturation of conductivity at high temperature is a typical behavior for doped semiconductors and indicates exhaustion of carriers (all available defects are ionized) [20]. For the reduced acceptor-doped samples with divalent acceptor states (Fe^{2+}), the available defect concentration will be the difference between the oxygen vacancy and the acceptor concentration. For a conductivity of $\sigma = 0.01 - 0.1$ S/cm this corresponds to $n = [\mathrm{V_O}] - [\mathrm{Fe_{Ti}}] \approx 10^{18}$ cm^{-3}, which is about 0.33 % of the total acceptor (and oxygen vacancy) concentration for 0.5 wt.% doping. A simulation of the temperature dependent conductivity of such a highly compensated semiconductor ($n \ll [\mathrm{V_O}] \approx [\mathrm{Fe_{Ti}}]$), did not reproduce the temperature dependence with any reasonable set of parameters, as shown in Figure 10(a). We can exclude that the saturation is caused by a starting incorporation of oxygen as the behavior is reproducible during heating and subsequent cooling. We currently speculate that the specific temperature dependence of the conductivity of the reduced Fe-doped samples with a saturation at higher temperature is caused by a redistribution of oxygen vacancies between the interior of the grains and the space-charge regions at the grain boundaries as sketched in Figure 10(b). Within this explanation, at high temperature the oxygen vacancy inside the bulk of the grain would have to be slightly higher than the Fe concentration and have to decrease below the Fe concentration with decreasing temperature. Two effects would contribute to such a redistribution: i) the temperature dependence of permittivity will change the width of the space-charge region, and ii)

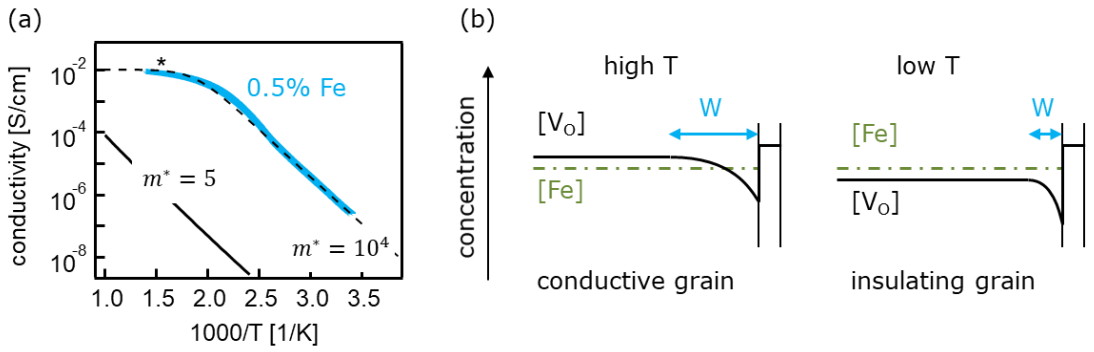

Figure 10: (a) Temperature dependence of a reduced 0.5 wt.% Fe-doped $BaTiO_3$ with simulated temperature dependence of conductivity assuming a highly compensated semiconductor, an activation energy of 0.4 eV, and a constant carrier mobility of 0.1 cm^2/Vs. Using the know effective mass of $BaTiO_3$ of 5 m_e, the conductivity is severely underestimated. Reasonable agreement is only obtained an effective mass of 10^4 m_e, which is not conserved to be realistic. The saturation may be related to a temperature dependent redistribution of oxygen vacancies as sketched in (b).

the depletion of oxygen vacancies in the space-charge region depends on the factor $\exp\frac{\Delta\phi}{kT}$, where $\Delta\phi$ is the difference in electrostatic potential from its value in the bulk. Our current simulations (see below) do only take a redistribution of oxygen vacancies between the space-charge region and the grain boundary core into account, but not an exchange of oxygen vacancies with the grain interior. The latter is fixed in the simulations. An estimation reveals that the space-charge region provides a sufficient reservoir for changing the conductivity. For a cubic grain of 1 µm extension, a 5 nm wide space-charge region at the surface of the grain contains about 3 % of all atoms and for a homogeneous distribution and, consequently, also 3% of all oxygen vacancies. This is about 10 times the electronic carrier concentration of the sample at 400°C. With the known oxygen vacancy diffusivity [21], the redistribution of oxygen vacancies inside a 1 µm grain at 200 °C takes less than 100 seconds according to $\tau = \frac{L^2}{2D}$. Therefore, the distribution of oxygen vacancies inside the grain should be close to equilibrium at 200°C or higher. Such an internal redistribution of oxygen vacancies is also consistent with the higher room temperature conductivity of the 0.1 wt.% Fe-doped sample as compared to the 0.5 wt.% doped one, as the lower doped sample exhibits a much larger grains than the higher doped one.

vi. The non-Arrhenius-like behavior of conductivity in the vicinity the phase transition temperature, which can be observed at lower conductivity in all samples is likely related to the temperature dependence of the dielectric permittivity. On the one hand, this leads to charging/discharging currents of the capacitors due to the (relatively) fast temperature ramping. On the other hand, the permittivity also affects the width of the space-charge region (see section on Schottky barrier below). We have not yet attempted to quantify this effect.

4.3 Simulation of electrical conductivity

In order to reveal whether defect energy levels can be extracted from the conductivity measurements, we have performed defect chemical calculations for polycrystalline samples. In the simulations we solve the one-dimensional Poisson equation including segregation of oxygen vacancies to the grain boundary core using the model and procedure outlined by De Souza [7]. The equilibrium distribution of oxygen vacancies is obtained by means of an iterative procedure for a given enthalpy of segregation Δg. As Δg is not known,

we have varied it between −1 and −2 eV. The calculations were then performed as a function of the oxygen vacancy concentration in the interior of the grains, which has been stepwise up to two times the concentration of acceptor dopants. We have used the defect energies provided by Wechsler and Klein [18] for the Mn and Fe acceptors and the oxygen vacancies. The used values are listed in Table 1. The value for $Fe^{2+/3}$-transition is consistent with our single crystal measurements [6].

Table 1: Defect energy levels of acceptor-doped $BaTiO_3$ according to Wechsler and Klein [18], which have been used in the simulations of electrical conductivity of polycrystalline samples. A band gap of 3-1 eV is assumed.

	$Fe^{3+/4+}$	$Fe^{2+/3+}$	$Mn^{3+/4+}$	$Mn^{2+/3+}$	$V_O^{+/2+}$	$V_O^{0/+}$
$E-E_{VB}$ [eV]	0.8	2.4	1.2	1.9	2.9	3.05

To calculate the electrical conductivity of the samples, we considered only electrons in the conduction band and holes in the valence band. Oxygen ion conduction is excluded, as they do not contribute to the current signal in our dc-measurement configuration. For the electron and hole mobilities we have used those summarized by Maier and Randall [21]. As the segregation of oxygen vacancies to grain boundaries generates a positive charge in the grain boundary core, the energy bands bend downward towards the grain boundary. This results in an electron accumulation in the space-charge region, which generates a parallel conduction path for electrons. In order to take this into account, we have obtained the total electron conductivity by integrating the electron concentration along the cross-section of a grain. In accordance with the grain sizes obtained from electron microscopy, we have used grain sizes of 500 nm and of 12.5 µm for the 0.5 and 0.1 wt.% doped samples, respectively. The conductivity of holes requires a different treatment, as the holes have to overcome a potential barrier when transferring from one grain to another. For this purpose, we have employed the approach of De Souza [7], which is effectively an integration along a path of infinitesimal resistors, whose resistances are determined by the local hole concentration. For certain conditions, this results in an effective activation energy of hole transport, which approximately equals to the sum of the activation of hole transport in the bulk (determined by the Fermi energy and defect energy levels in the bulk) and the potential barrier at the grain boundary (determined by the band bending). The activation energy is obtained by calculating the conductivity at a second temperature, which is 20 K lower than the target temperature.

Figure 11 displays the simulated electrical conductivities and activation energies of the 0.1 and 0.5 wt.% Mn- and Fe-doped samples as a function of the oxygen vacancy concentration for different values of Δg. The three regions of conductivity, which have already been discussed above for the grain boundary free bulk ($\Delta g = 0$ eV, see Figure 9) are still clearly discernible. For high concentrations of oxygen vacancies, corresponding to region I, the conductivities are dominated by the oxygen vacancies and do not exhibit any dependence on doping species, doping concentration, and enthalpy of segregation. As the conductivity of the grains themselves is high, the additional conduction along the grain boundaries has no noticeable influence on the conductivity and on the activation energy.

In region II, for intermediate concentrations of oxygen vacancies, the conductivities still do not depend much on the enthalpy of segregation. The influence is more pronounced for Mn doping, where changing the enthalpy of segregation from 0 eV to −2 eV increases the conductivity by about one order of magnitude. The stronger influence of Δg for Mn-doping is also related to the lower energy of the $Mn^{2+/3+}$ level as compared to the $Fe^{2+/3+}$ level, which results in a substantially lower bulk conductivity of the Mn-

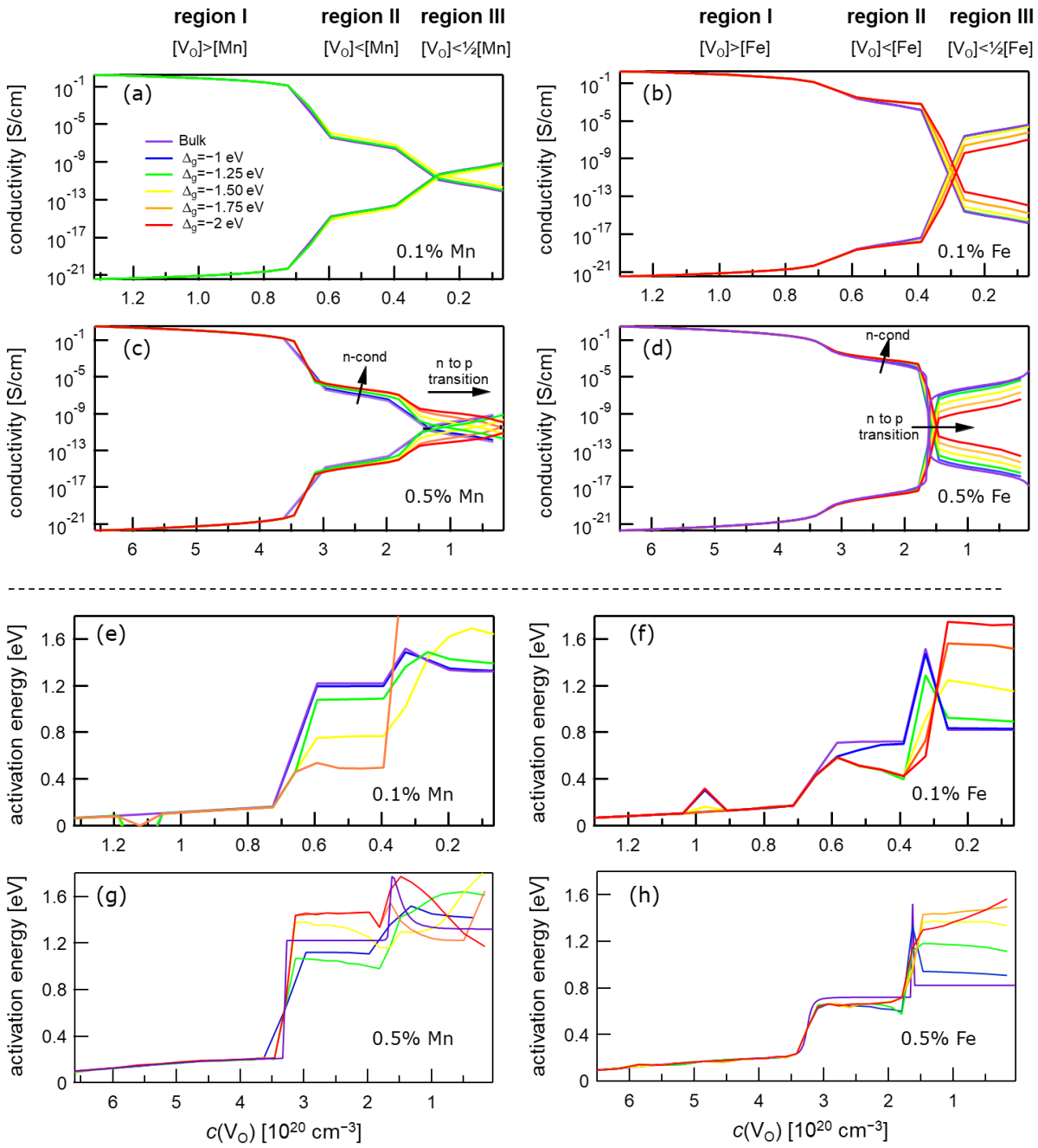

Figure 11: Electrical conductivities (a)-(d) and activation energies of conductivity (e)-(h) for 0.1 and 0.5 wt.% Mn-doped (left column) and Fe-doped (right column) polycrystalline $BaTiO_3$ calculated in dependence on oxygen vacancy concentration in the interior of the grains for different values of the free enthalpy of segregation of the oxygen vacancies, Δg. $\Delta g = 0$ corresponds to the bulk conductivity and is the same as those presented in Figure 9. All calculations shown are performed for a sample temperature of 400 °C.

doped samples in region II and consequently in a stronger influence of the electron conduction in the space-charge region. The simulated potential profiles illustrating the influence of the energy levels of the dopants and space-charge regions are displayed in Figure 12.

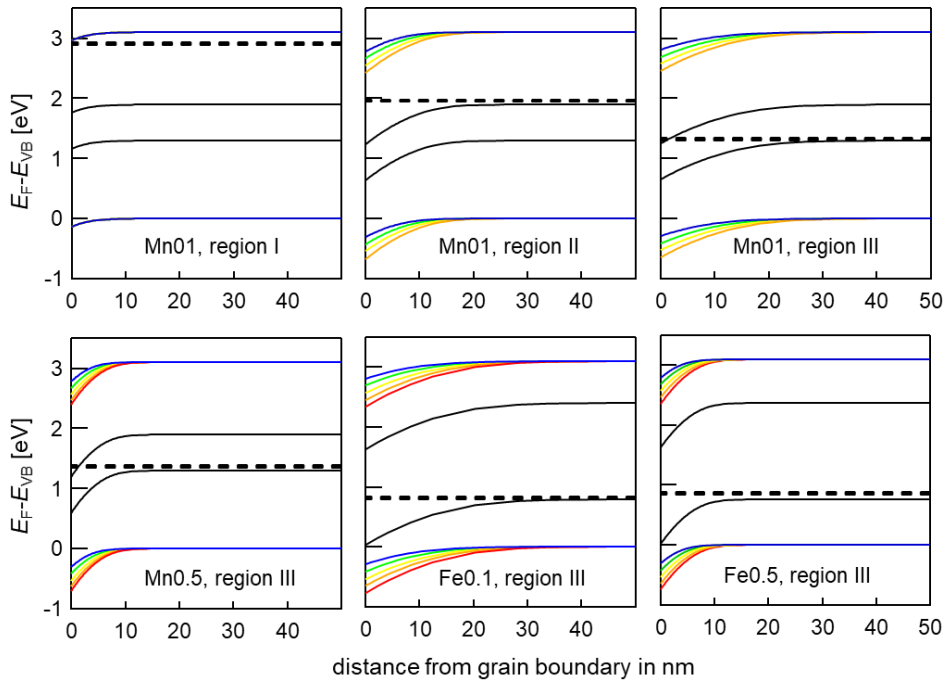

Figure 12: Calculated potential profiles for 0.1 wt.% Mn-doped $BaTiO_3$ for different concentrations of oxygen vacancies (top row). The selected vacancy concentrations correspond to regions I-III of the simulations. The bottom tow shows potential profiles for 0.5 wt.% Mn, 0.1 wt.% Fe, and 0.5 wt.% Fe-doped samples. All calculations are performed for a temperature of 400 °C.

The conduction in the space-charge region for intermediate concentrations of oxygen vacancies has a pronounced effect on the activation energy, particularly for the Mn-doped samples (see Figure 11(e) and (g)). For example, the activation energy in region II decreases from 1.2 eV for pure bulk conduction to 0.4 eV for the highest assumed enthalpy of segregation $\Delta g = -2$ eV. Due to this dependence, it is only possible to extract the energy of the $Mn^{2+/3+}$ level from the measured activation energy (which has been the goal of the measurements) if Δg is known with sufficient accuracy. This uncertainty is not there for the Fe dopants. Here, the activation energy is almost independent on Δg. This is due to the higher $Fe^{2+/3+}$ charge transition level, which results in a higher bulk conductivity of the Fe-doped samples in this region of oxygen vacancy concentrations. It should thus be possible to obtain the position of the $Fe^{2+/3+}$ level in the energy gap from the activation energy. This will not be possible at 400°C due to the saturation of conductivity. Simulations at lower temperatures are still ongoing. Too low temperatures cannot be used as this results in a too strong depletion of oxygen vacancies in the space-charge regions and a too high concentration in the grain boundary core. This situation cannot be treated without taking defect interactions into account [22].

In the strongly oxidized region III, the conductivity is mostly p-type with hole conduction dominating over electron conduction. An exception is the sample doped with 0.5 wt.% Mn. For higher enthalpies of segregation, electron conduction still dominates over p-type conduction. This happens as the energy levels of the $Mn^{2+/3+}$- and of the $Mn^{3+/4+}$-transition differ by only 0.7 eV (see Table 1). For higher enthalpies of segregation, the potential barrier at the grain boundaries decreases the hole conductivity and increases electron conduction in the space-charge regions. For the highest enthalpy of segregation, the band bending becomes so high, that Mn even becomes 2+ near the interface, as the Fermi energy crosses the $Mn^{2+/3+}$

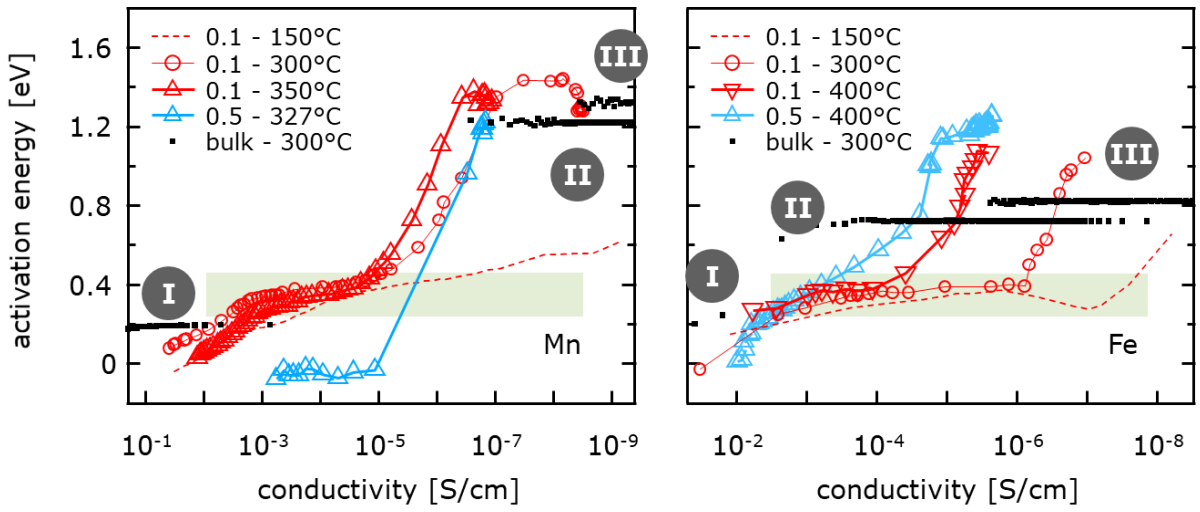

Figure 13: Activation energies as a function of conductivity of the 0.1 and 0.5 wt.% Mn-doped (left) and Fe-doped (right) polycrystalline $BaTiO_3$ bulk ceramics. The data are extracted from the measurements shown in Figure 8 at different temperatures. No data points are available for the 0.5 wt% Mn-doped sample at high conductivity, as the sample is already partially re-oxidized when it reaches 300 °C. The black dots correspond to the calculations for single crystalline material ($\Delta g = 0$ eV) at 400 °C. The numbers in the gray circles correspond to the regions of different oxygen vacancy concentrations for the simulated activation energies.

level in the space-charge region. Although this also happens for the 0.1 wt.% Mn-doped sample, the effect on the conductivity is less pronounced in this case, which is related to the larger grain size in the simulations. As electron and hole conductivities in region III are comparable for the Mn-doped samples, it will be difficult to distinguish between n- and p-type conductance.

The situation is different for the Fe-doped samples, for which the hole conductivity clearly dominates over the electron conductivity in region III. In this region, the Fermi level is pinned at the $Fe^{3+/4+}$ level, which is much closer to the valence band than to the conduction band. The $Fe^{3+/4+}$ level is also much closer to the valence band than the $Mn^{3+/4+}$ level. Consequently, the conductivity in region III is higher for the Fe-doped samples (10^{-8}–10^{-6} S/cm) than for the Mn-doped ones (10^{-12}–10^{-9} S/cm). This difference is related to the degradation behavior, as region III is the region with the lowest conductivity, which dominates the leakage current of degraded samples [11], [23]. It is therefore to be expected that Fe-doped samples exhibit a stronger increase in conductivity than Mn-doped ones.

4.4 Comparison of simulation and experiment

The calculated dependence of conductivity and activation energy on the oxygen vacancy concentration and on Δg can now be compared with the measurements shown in Figure 8 in order to evaluate whether the energy levels of the defects and enthalpy of segregation can be extracted from the measurements. For this purpose, the activation energies determined from various temperature cycles are plotted in Figure 13 as a function of the electrical conductivity. The same procedure allowed to extract the energy levels of the defects in the case of single crystalline samples [6] (see Figure 5).

The comparison is started for the 0.5 wt.% Mn-doped sample. In this case, the abrupt jump in conductivity and activation energy indicates a transition from region I ($[V_O]>[Mn_{Ti}]$) to region II, similar to the Fe-doped $SrTiO_3$ single crystal. The conductivity of 10^{-7} S/cm and the activation energy of 1.2 eV are both in good

agreement with the calculations for $\Delta g = 0$ and a $Mn^{2+/3+}$ level as given in Table 1. In contrast to the 0.5 wt.% Mn-doped sample, the conductivity of the 0.1 wt.% Mn-doped sample decreases and its activation energy increases gradually in the course of re-oxidation. At a conductivity of 10^{-7} S/cm, corresponding to region II, the activation energy at 300 °C and 350 °C both exhibits values slightly higher than 1.3 eV. That the activation energy is slightly higher than expected for a defect energy level 1.2 eV below the conduction band, may lead to a small correction of this value.

The activation energy of the 0.1 wt.% Mn-doped sample extracted at different temperatures exhibits a plateau at 0.35−0.4 eV, as indicated by the green region in Figure 13. The plateau of the activation energy would be consistent with a rather large value of $\Delta g \leq -1.75$ eV in region II, but the conductivity is still too high to assign the activation energy to that region. A similar gradual increase of conductivity and activation energy has also been observed for a second 0.1 wt.% Mn-doped sample, a 0.05 wt.% Mn-doped, a nominally undoped, and also for both Fe-doped samples (see also Figure 13). This activation energy of 0.4 eV is the same as that of the reduced Fe-doped samples at lower temperature (see Figure 10). While the saturation of conductivity for the reduced Fe-doped samples at high temperature might be explained by a redistribution of oxygen vacancies as sketched in Figure 10(b), the redistribution cannot explain the activation energy of 0.4 eV. As this activation energy is common for Fe-doped and the 0.1 wt.% Mn-doped $BaTiO_3$, it is unlikely that it is related to a specific defect energy level. For the 0.1 wt.% Mn-doped sample it might be consistent with the Mn defect energy level and a very high enthalpy of segregation of the oxygen vacancies of $\Delta g \approx -2$ eV. However, such a high value differs considerably from that derived by De Souza for an acceptor-doped $SrTiO_3$ bicrystal [7]. The other samples also provide no evidence for such a high enthalpy of segregation. It is therefore concluded that the simulations of electrical conductivity do not yet take all effects contributing to the electrical properties of the studied samples into account. This is furthermore evident from the activation energies of the Fe-doped samples. These show no plateaus at the expected defect energy levels, which are consistent throughout literature [6][18][19]. Effects, which might be considered in addition are i) the temperature dependent redistribution of oxygen vacancies between the grain boundary core, the space-charge region, and the grain interior, ii) the segregation of cation vacancies and dopants to the grain boundary core, which would modify the core-charge and thereby the space-charge potential, and iii) a partial incorporation of oxygen vacancies throughout the sample. The latter has been observed for partially re-oxidized samples [24][25]. In order to obtain a better understanding of the electrical properties of acceptor-doped polycrystalline $BaTiO_3$, the effects mentioned above need to be included in the simulations. In addition, a different experimental procedure to vary the oxygen content can be applied. It will be advantageous but experimentally more demanding and time-consuming to equilibrate the oxygen content of the samples at high temperature with gradual variation of the oxygen partial pressure ranging from 1 to 10^{-22} bar or more and measure the activation energy at low temperature after each equilibration step.

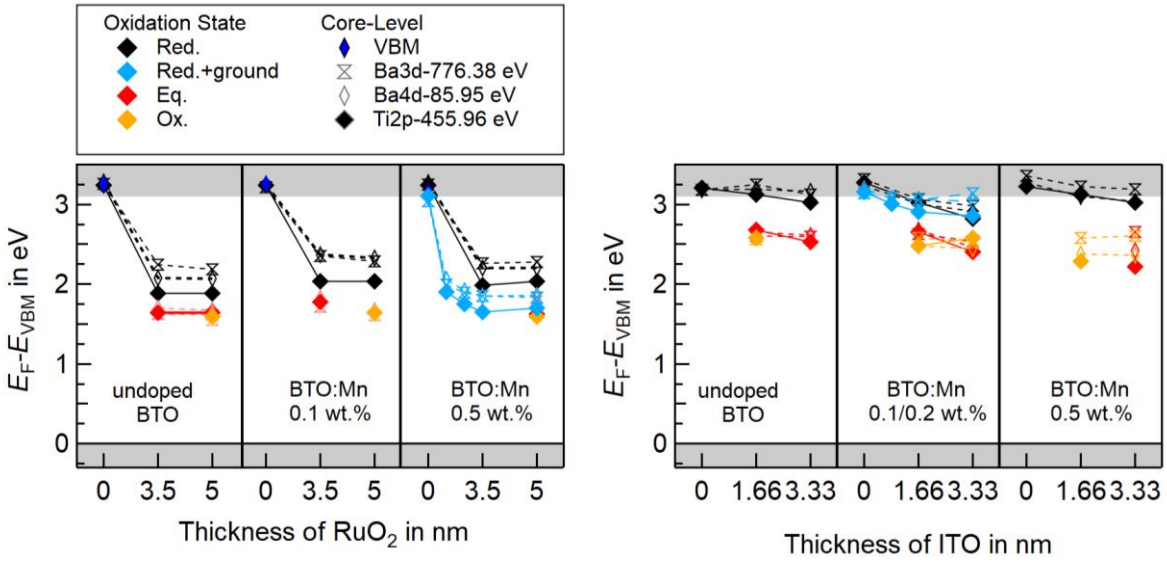

Figure 14: Evolution of valence band maximum binding energy E_F- E_{VBM} with increasing RuO_2 (left) and ITO (right) thickness for undoped, 0.1 wt.% and 0.5 wt.% Mn-doped $BaTiO_3$ ceramics in an oxidized (orange), equilibrated (red) and reduced state (black). The interface of reduced Mn-doped samples (RuO_2: 0.5 wt.% Mn, ITO: 0.2 wt.% Mn) after removal of the surface layer are also included (blue). Dashed lines connect values derived from the Ba *3d* and *4d* emissions and solid lines to those from Ti *2p* emissions.

5 Analysis of Schottky barrier heights at $BaTiO_3$ interfaces

The second main part of this project has been the determination of Schottky barrier heights in dependence on doping concentration by means of X-ray photoelectron spectroscopy. Due to earlier availability of samples, we have chosen Mn-doped $BaTiO_3$ for a systematic study of the dependence of barrier height on doping concentration and sample condition. For this purpose, we used nominally undoped, 0.1 and 0.5 wt.% Mn-doped $BaTiO_3$. Different oxygen vacancy concentrations of the substrates have been realized by using reduced, equilibrated and oxidized samples. Due to the formation of a Ba-rich surface after reduction, some samples were ground after reduction before deposition of the contact material. Oxidized samples were treated by exposure to an atomic oxygen flux from a tectra Gen II source in the vacuum system. To provide a high variation of the Fermi energy at the interface, we have used RuO_2 as a high work function material and ITO as a low work function material. Oxides were chosen as contact materials instead of metals to avoid interfacial reactions, particularly the generation of oxygen vacancies [26]. As the equilibrated and oxidized samples are not sufficiently conductive, no Fermi energies can be extracted before deposition of the contact material. All reduced samples exhibit a Fermi energy near a slightly above the conduction band minimum. This is consistent with the high electrical conductivity of the samples. The evolution of the Fermi energy at the different interfaces is summarized in Figure 14.

The data in Figure 14 show the Fermi level positions derived from the valence band maximum and from the three accessible core levels of $BaTiO_3$, Ba 3*d*, 4*d* and Ti 2*p*. For the RuO_2 interfaces, the Ti 2*p* levels of the reduced samples experiences larger shifts than the Ba levels. This is related to the Ba-rich surface phase, which results in different areas probed by the Ba and the Ti levels. After grinding the Ba-rich surface, all core levels exhibit almost identical shifts. It also appears that the reduced samples have higher Fermi energies at the interfaces. In the case of RuO_2, the difference disappears after removal of the surface layer.

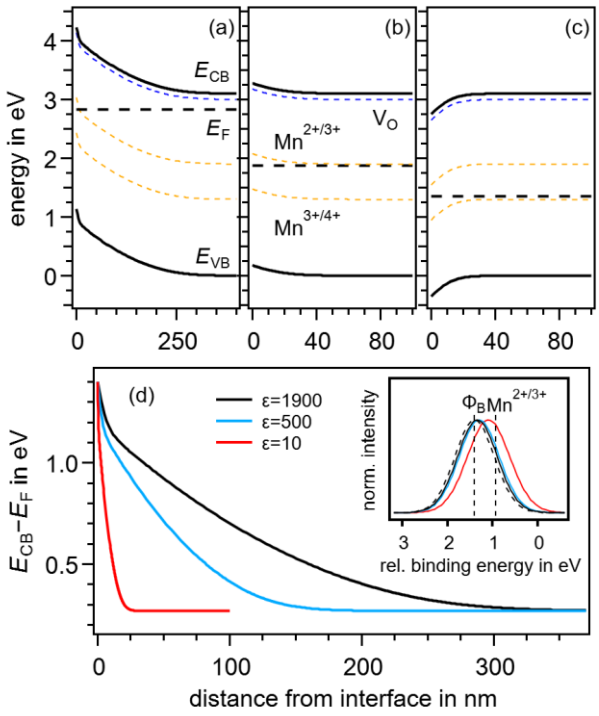

Figure 15: Simulated energy band diagrams for $BaTiO_3$ doped with 3.3×10^{20} cm^{-3} Mn. The concentrations of oxygen vacancies are 3.31×10^{20} cm^{-3} (a), 1.83×10^{20} cm^{-3} (b), and 1.0×10^{20} cm^{-3} (c), respectively. The energy is referenced to the valence band maximum positions in the bulk. The variation of the conduction band energy E_{CB} for the conditions given in (a) but for different relative permittivity ε is shown in (d). Simulated core level spectra are shown in the insert of (d). Here, the dashed grey spectrum corresponds to a Gaussian peak with a full width at half maximum of 1 eV for a flat potential with E_{CB} = 1.4 eV. The black, blue and red spectra correspond to the spectra induced by the potential profiles shown in (d) for an inelastic mean free path of the photoelectrons of 2 nm. The two dashed vertical lines in the insert correspond to the position of the Fermi energy at the interface and to that of the $Mn^{2+/3+}$ charge transition level assumed in the simulations.

Eventually, the Fermi energy at the $BaTiO_3/RuO_2$ interface is at $E_F - E_{VB} = 1.7$ eV, independent on doping and oxygen vacancy concentration. It has been expected that the Fermi energy is pinned at the defect energy levels, which would enable the determination of the defect energy from the measurements. This is evidently not the case.

In order to understand why no Fermi level pinning at the defect levels is observed at the interfaces, we have solved the Poisson equation for 0.5 wt.% Mn-doped $BaTiO_3$ and an interface Fermi energy as observed at the $BaTiO_3/RuO_2$ interface. The latter is in between the $Mn^{2+/3+}$ and the $Mn^{3+/4+}$ charge transition levels, which were the same as those used for the conductivity simulations (see Table 1). Bulk oxygen vacancy concentrations have been selected to be representative for the regions I to III described in section 2. 4. This leads to bulk Fermi energies being close the conduction band as in Figure 15(a), close to the $Mn^{2+/3+}$ transition as in Figure 15(b), or close to the $Mn^{3+/4+}$ transition as in Figure 15(c), respectively. For the highest concentration of oxygen vacancies, the $Mn^{2+/3+}$ level crosses the Fermi energy in the space-charge region. As this leads to a change of charge density in the space-charge region, the curvature of the energy bands changes at the crossover position. Fermi level pinning at the $Mn^{2+/3+}$ level would be observed if the information depth of the photoelectrons becomes comparable to extension of the space-charge region in the steeper part of band bending. This is clearly not the case. The reason lies in the high permittivity of $BaTiO_3$, which increases the extension of the space-charge region. This is confirmed by simulations performed with different relative permittivity, which are displayed in Figure 15(d). Only for the lowest permittivity of $\varepsilon = 10$, a shift of the peak position towards the defect's energy level is observed (see inset of Figure 15). The photoemission spectra were obtained using a convolution of spectra having a relative binding energy as obtained from the potential distribution and intensity according to an exponential attenuation with the inelastic mean free path of the photoelectrons. On the one hand, the simulations reveal that a pinning, and the related determination of the defect energy levels, becomes observable

either for much higher defect concentrations or for materials with lower permittivity. On the other hand, it becomes clear that a higher permittivity results in a larger effect of grain boundaries on the electrical properties of polycrystalline materials.

The Fermi energies at the $BaTiO_3$/ITO interfaces, which are shown in the right graph of Figure 14, are different for the reduced and the oxidized samples. In contrast to the interfaces with RuO_2, this difference remains for an interface measured after removal of the Ba-rich surface layer. This is not expected in the light of the simulations of the potential profiles described in the previous paragraph. We assign the difference to the fact that the ITO films were deposited at room temperature. Such films have an electrical conductivity, which is two orders of magnitude lower than those of films deposited at 400 °C [27]. The low carrier concentration and film thickness may thus not provide sufficient charge to compensate for the high space-charge density in the reduced substrate. Deposition of ITO at higher substrate temperature is still ongoing.

6 In-situ degradation studies

It has been planned to perform in-operando studies of resistance degradation using X-ray photoelectron spectroscopy. For this purpose, an available sample manipulator and an available heating stage have been combined during the course of the project. The heating stage became available at the end of 2020 and was installed in the XPS system early 2021. Due to difficulties experienced during installation and testing and a total failure of the air condition of the lab, operation could not be started before July 2021. Therefore, it has not been possible to perform for test measurements within the period of this project.

References

[1] H. Kishi, Y. Mizuno, and H. Chazono, "Base-Metal Electrode-Multilayer Ceramic Capacitors: Past, Present and Future Perspectives," *Jpn. J. Appl. Phys.*, vol. 42, no. 1R, pp. 1–15, 2003.

[2] K. Hong, T. H. Lee, J. M. Suh, S.-H. Yoon, and H. W. Jang, "Perspectives and challenges in multilayer ceramic capacitors for next generation electronics," *J. Mater. Chem. C*, vol. 7, no. 32, pp. 9782–9802, 2019, doi: 10.1039/C9TC02921D.

[3] T. Baiatu, R. Waser, and K.-H. Härdtl, "dc Electrical Degradation of Perovskite-Type Titanates: III, A Model of the Mechanism," *J. Am. Ceram. Soc.*, vol. 73, no. 6, pp. 1663–1673, 1990, doi: 10.1111/j.1151-2916.1990.tb09811.x.

[4] S. Rodewald, N. Sakai, K. Yamaji, H. Yokokawa, J. Fleig, and J. Maier, "The Effect of the Oxygen Exchange at Electrodes on the High-Voltage Electrocoloration of Fe-Doped $SrTiO_3$ Single Crystals: A Combined SIMS and Microelectrode Impedance Study," *J. Electroceramics*, vol. 7, no. 2, pp. 95–105, 2001, doi: 10.1023/B:JECR.0000027949.32661.9d.

[5] M. Wojtyniak, K. Szot, R. Wrzalik, C. Rodenbücher, G. Roth, and R. Waser, "Electro-degradation and resistive switching of Fe-doped SrTiO3 single crystal," *J. Appl. Phys.*, vol. 113, no. 8, p. 83713, 2013, doi: 10.1063/1.4793632.

[6] I. Suzuki and L. Gura, "The energy level of the $Fe^{2+/3+}$-transition in $BaTiO_3$ and $SrTiO_3$ single crystals," *Phys. Chem. Chem. Phys.*, vol. 21, pp. 6238–6246, 2019, doi: 10.1039/C8CP07872F.

[7] R. A. De Souza, "The formation of equilibrium space-charge zones at grain boundaries in the perovskite oxide $SrTiO_3$," *Phys. Chem. Chem. Phys.*, vol. 11, pp. 9939–9969, 2009, doi: 10.1039/b904100a.

[8] S. Siol *et al.*, "Band Alignment Engineering at Cu_2O/ZnO Heterointerfaces," *ACS Appl. Mater. Interfaces*, vol. 8, pp. 21824–21831, 2016, doi: 10.1021/acsami.6b07325.

[9] R. M. Glaister and H. F. Kay, "An Investigation of the Cubic-Hexagonal Transition in Barium Titanate," *Proc. Phys. Soc.*, vol. 76, no. 5, pp. 763–771, 1960, doi: 10.1088/0370-1328/76/5/317.

[10] H.-J. Hagemann and H. Ihrig, "Valence change and phase stability of 3d-doped $BaTi_3$ annealed in oxygen and hydrogen," *Phys. Rev. B*, vol. 20, no. 9, pp. 3871–3878, 1979, doi: 10.1103/PhysRevB.20.3871.

[11] J.-J. Wang *et al.*, "Defect Chemistry and Resistance Degradation in Fe-doped $SrTiO_3$ Single Crystal," *Acta Mater.*, vol. 108, pp. 229–240, 2016, doi: 10.1016/j.actamat.2016.02.022.

[12] S.-H. Yoon, C. A. Randall, and K.-H. Hur, "Difference between resistance degradation of fixed valence acceptor (Mg) and variable valence acceptor (Mn)-doped $BaTiO_3$ ceramics," *J. Appl. Phys.*, vol. 108, no. 6, p. 64101, 2010, doi: 10.1063/1.3480992.

[13] K. N. S. Schuldt, H. Ding, J.-C. Jaud, J. Koruza, and A. Klein, "Influence of defects on the Schottky barrier height at $BaTiO_3/RuO_2$ interfaces," *Phys. Status Solidi*, 2021, doi: 10.1002/pssa.202100143.

[14] R. Meyer, R. Waser, J. Helmbold, and G. Borchardt, "Cationic Surface Segregation in Donor-Doped $SrTiO_3$ Under Oxidizing Conditions," *J. Electroceramics*, vol. 9, no. 2, pp. 101–110, 2002, doi: 10.1023/A:1022898104375.

[15] R. Schafranek, S. Payan, M. Maglione, and A. Klein, "Barrier heights at $(Ba,Sr)TiO_3$/Pt interfaces studied by photoemission," *Phys. Rev. B*, vol. 77, p. 195310, 2008, doi: 10.1103/PhysRevB.77.195310.

[16] S. Li, C. Ghinea, T. J. M. Bayer, M. Motzko, R. Schafranek, and A. Klein, "Electrical properties of $(Ba,Sr)TiO_3$ thin films with Pt and ITO electrodes: Dielectric and rectifying behaviour," *J. Phys. Condens. Matter*, vol. 23, p. 334202, 2011, doi: 10.1088/0953-8984/23/33/334202.

[17] J. Maier, *Physical Chemistry of Ionic Materials*. Weinheim: Wiley-VCH, 2004.

[18] B. A. Wechsler and M. B. Klein, "Thermodynamic point defect model of barium titanate and application to the photorefractive effect," *J. Opt. Soc. Am. B*, vol. 5, p. 1711, 1988, doi: 10.1364/JOSAB.5.001711.

[19] H.-J. Hagemann and D. Hennings, "Reversible Weight Change of Acceptor-Doped $BaTiO_3$," *J. Am. Ceram. Soc.*, vol. 64, no. 10, pp. 590–594, 1981, doi: 10.1111/j.1151-2916.1981.tb10223.x.

[20] S. M. Sze and K. K. Ng, *Physics of Semiconductor Devices*. Hoboken: John Wiley & Sons, 2007.

[21] R. A. Maier and C. A. Randall, "Low Temperature Ionic Conductivity of an Acceptor-Doped Perovskite: II. Impedance of Single-Crystal $BaTiO_3$," *J. Am. Ceram. Soc.*, vol. 99, no. 10, pp. 3360–3366, 2016, doi: 10.1111/jace.14347.

[22] A. F. Zurhelle, X. Tong, A. Klein, D. S. Mebane, and R. A. De Souza, "A space-charge treatment of the increased concentration of reactive Ce^{3+} at the surface of a ceria solid solution," *Angew. Chemie Int. Ed.*, vol. 56, no. 46, pp. 14516–14520, 2017, doi: 10.1002/anie.201708118.

[23] T. J. M. Bayer, J. J. Carter, J.-J. Wang, A. Klein, L.-Q. Chen, and C. A. Randall, "Determination of electrical properties of degraded mixed ionic conductors: Impedance studies with applied dc voltage," *J. Appl. Phys.*, vol. 122, no. 24, p. 244101, 2017, doi: 10.1063/1.5006062.

[24] C. Schaffrin, "Oxygen diffusion in $BaTiO_3$ ceramic," *Phys. Status Solidi*, vol. 35, no. 1, pp. 79–88, 1976, doi: 10.1002/pssa.2210350109.

[25] K. Watanabe, I. Sakaguchi, S. Hishita, N. Ohashi, and H. Haneda, "Visualization of Grain Boundary as Blocking Layer for Oxygen Tracer Diffusion and a Proposed Defect Model in Non Doped $BaTiO_3$ Ceramics," *Appl. Phys. Express*, vol. 4, no. 5, p. 55801, 2011, doi: 10.1143/APEX.4.055801.

[26] A. Klein, "Interface Properties of Dielectric Oxides," *J. Am. Ceram. Soc.*, vol. 99, pp. 369–387, 2016, doi: 10.1111/jace.14074.

[27] C. Lohaus, C. Steinert, G. Deyu, J. Brötz, W. Jaegermann, and A. Klein, "Enhancing electrical conductivity of room temperature deposited Sn-doped In_2O_3 thin films by hematite seed layers," *Appl. Phys. Lett.*, vol. 112, no. 15, p. 152105, Apr. 2018, doi: 10.1063/1.5022683.

Publications

[1] I. Suzuki, L. Gura, and A. Klein, "The energy level of the $Fe^{3+/2+}$ transition in $BaTiO_3$ and $SrTiO_3$ single crystals" Phys. Chem. Chem. Phys. Vol. 21, p. 6283, 2019, doi: 10.1039/C8CP07872F

[2] K.N.S. Schuldt, H. Ding, J.-C. Jaud, J. Koruza, and A. Klein, "Influence of defects on the Schottky barrier height at $BaTiO_3/RuO_2$ interfaces", *phys. stat. sol. (a)*, vol. 218, p. 2100143, 2021, doi: 10.1002/pssa.202100143.

Contributed Theses

Katharina Schuldt PhD student, funded by AFORL, thesis in progress

Lisanne Gossel Master Thesis (2020): *Influence of Grain Boundaries and Defect Energy Levels on the Electrical Properties of Acceptor-doped Polycrystalline $BaTiO_3$*

Baris Öcal Master Thesis (2019): *Effect of ITO anode on resistance degradation of $BaTiO_3$*

Nicola Gutmann Bachelor thesis (2019): *Influence of Mn-doping on the electrical properties of polycrystalline $BaTiO_3$*

Hui Ding Master Thesis (2018): *Electrical Studies of Acceptor-doped $BaTiO_3$*

Disclaimer

Any opinions, findings, and conclusions or recommendations expressed in this report are those of the author(s) and do not necessarily reflect the views of the Air Force Office of Scientific Research, Air Force Materiel Command, USAF.